Engineering band structure via dual atoms modification for the efficient photoanode

Xiaodong Wang [a,1], Huijuan Zhang [a,b,1],Chuanzhen Feng [a], Yu Wang [a,b]*

[a] The School of Chemistry and Chemical Engineering, National Key Laboratory of Power Transmission Equipment Technology, Chongqing University, 174 Shazheng Street, Shapingba District, Chongqing City, 400044, P.R. China

[b] College of Chemistry and Environmental Science, Inner Mongolia Normal University, Huhehaote, 010022, P. R. China

[1] These authors contributed equally to this work.
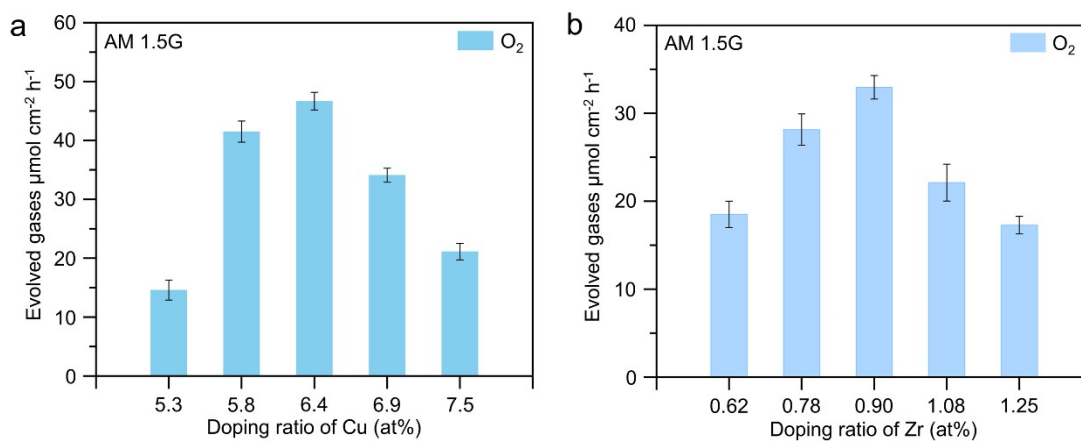
E-mail address: wangy@cqu.edu.cn

Figure S1. O_2 evolution amount in different a) Cu doping Ta_3N_5 and b) Zr doping Ta_3N_5, respectively. Error bars are the standard deviation. Both photoelectrodes were loaded with cocatalyst NiCoFe-B$_i$. Then, the NiCoFe-B$_i$/Cu-Ta_3N_5/FTO and NiCoFe-B$_i$/Zr-Ta_3N_5/FTO photoanode were held at 1.0 V_{RHE} in 1 M KOH under AM 1.5G simulated sunlight for 1 h.
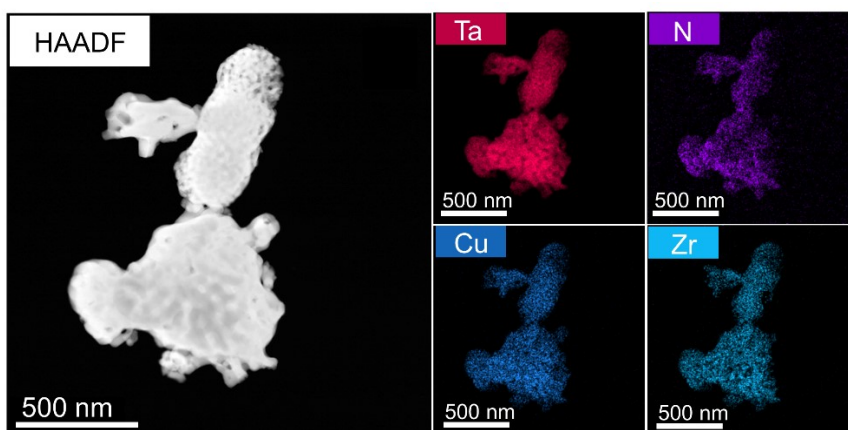
Figure S2. HAADF-STEM image of Cu,Zr$_h$-Ta$_3$N$_5$ and Corresponding EDS elemental mappings.

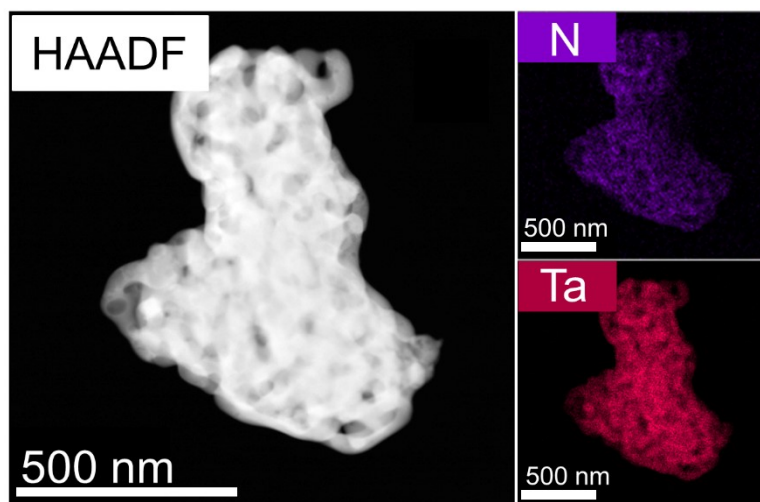Cu,Zr$_h$-Ta$_3$N$_5$ synthesized by conventional methods shows a uniform distribution of Zr.

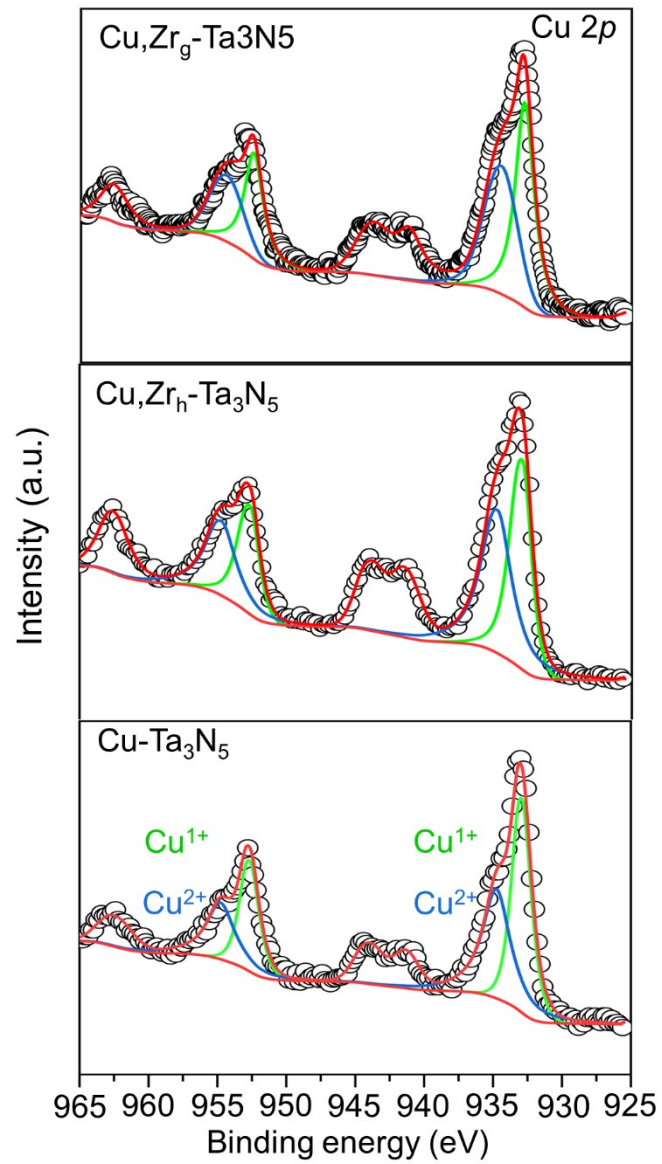Figure S3. HAADF-STEM image of pristine Ta$_3$N$_5$ and Corresponding EDS elemental mappings.

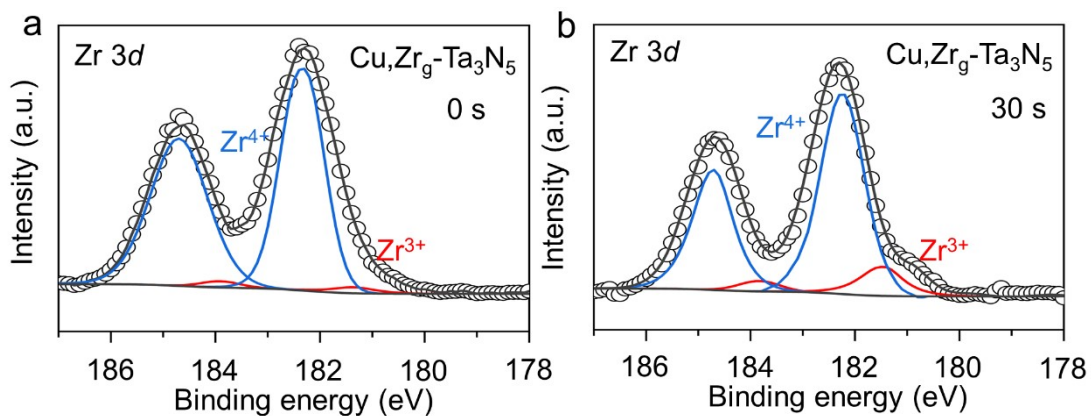Figure S4. Cu 2*p* high-resolution XPS spectra of Cu-Ta$_3$N$_5$, Cu,Zr$_h$-Ta$_3$N$_5$ and Cu,Zr$_g$-Ta$_3$N$_5$.

Figure S5. Zr $3d$ High-resolution XPS spectra of Cu,Zr$_g$-Ta$_3$N$_5$ under different etching times, a) 0 s and b) 30 s.

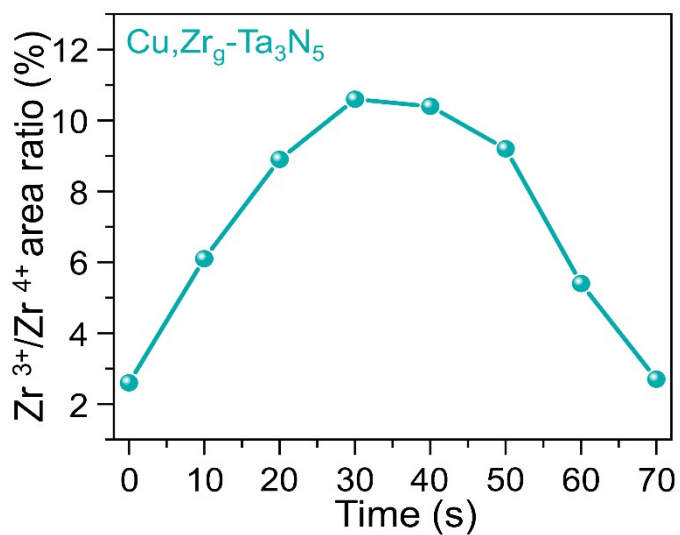Figure S6. Zr^{3+}/Zr^{4+} area ratio of Cu,Zr$_g$-Ta$_3$N$_5$ vs etching time obtained from XPS measurements. The volcano-shaped curve indicates that the Zr^{3+}/Zr^{4+} area ratio follows the regularity of gradient changes.
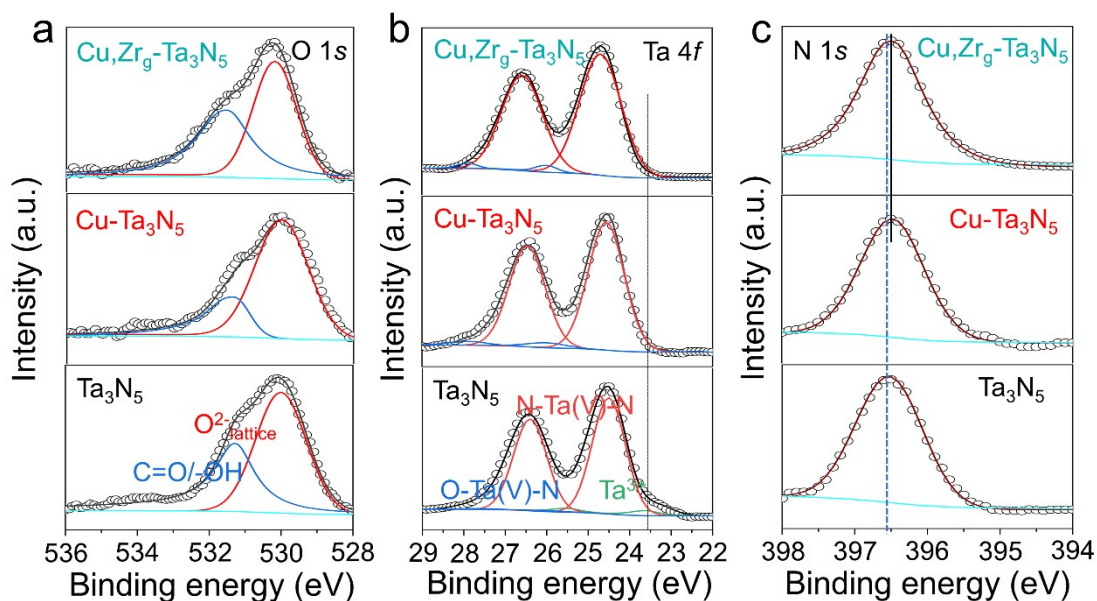
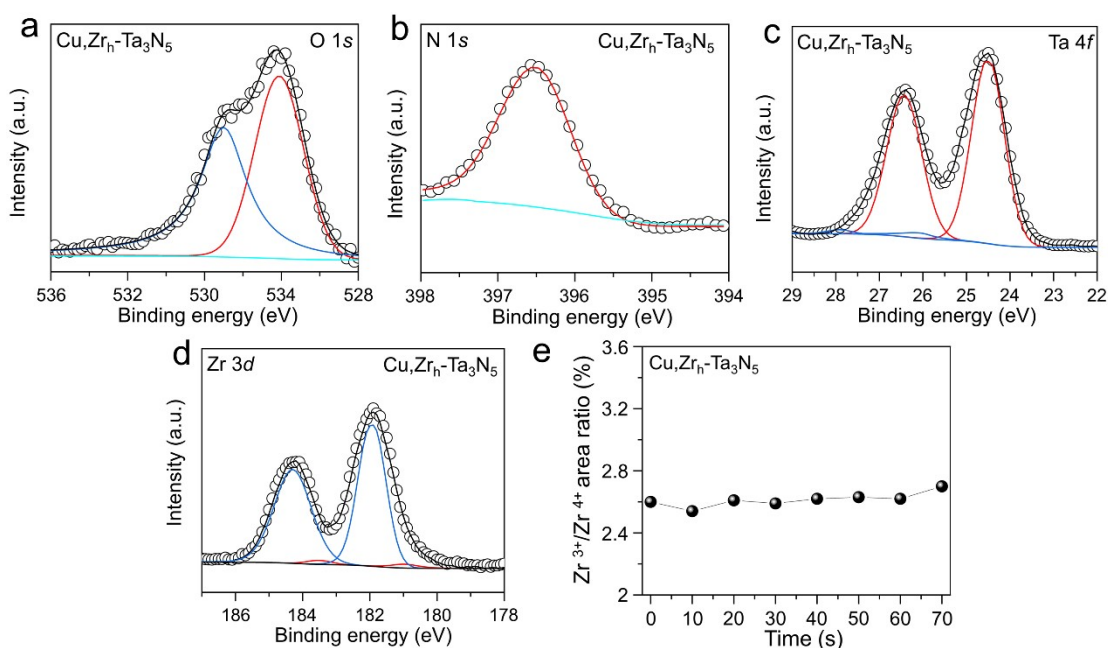Figure S7. a) O 1*s*; b) Ta 4*f* and c) N 1*s* high-resolution XPS spectra of Ta_3N_5, $Cu-Ta_3N_5$ and Cu,Zr_g-Ta_3N_5.

Figure S8. a) O 1*s*; b) N 1*s*; c) Ta 4*f*; d) Zr 3*d* high-resolution XPS spectra of Cu,Zr_h-Ta_3N_5 and e) Zr^{3+}/Zr^{4+} area ratio of Cu,Zr_h-Ta_3N_5 vs etching time obtained from XPS measurements. As shown in Figure R1, according to the XPS etching curve, it can be seen that the ratio of Zr^{3+} and Zr^{4+} changes little over time, indicating that the interaction of Cu and Zr in Cu,Zr_h-Ta_3N_5 is similar. In addition, we made a change in the supporting information and marked it in red.
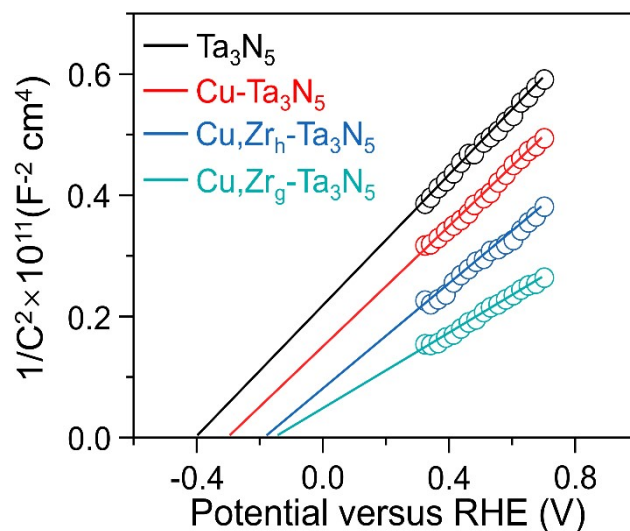
Figure S9. Mott–Schottky plot for Ta_3N_5, Cu-Ta_3N_5, Cu,Zr_h-Ta_3N_5 and Cu,Zr_g-Ta_3N_5 without co-catalyst under dark conditions. The M-S plot only exhibits the positive slope, suggesting its intrinsic n-type conductivity.
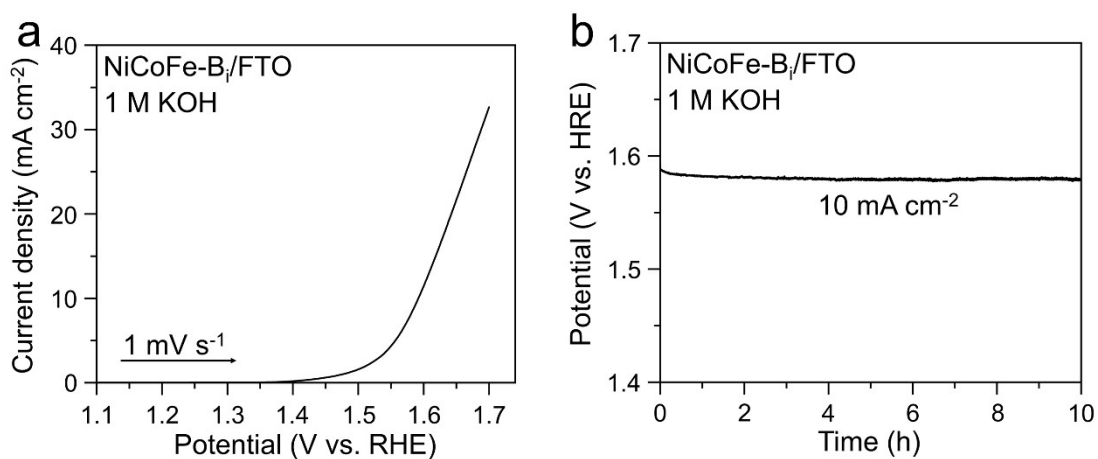

Figure S10. Electrocatalytic OER performance of NiCoFe-B_i catalyst deposited on FTO electrode in 1 M KOH. a) The OER polarization curve of the NiCoFe-B_i catalyst; b) Stability test of the NiCoFe-B_i catalyst on FTO measured at constant current density of 10 mA cm^{-2} for 10 h. The overpotential without iR correction.
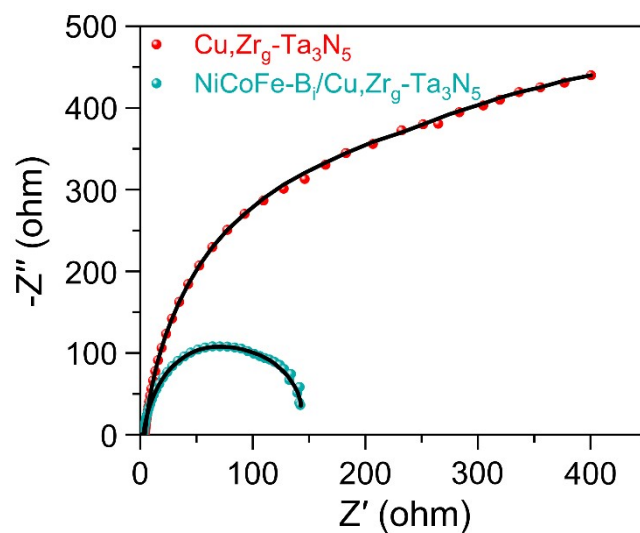
Figure S11. Electrochemical impedance spectra for $Cu,Zr_g-Ta_3N_5$ and $NiCoFe-B_i/Cu,Zr_g-Ta_3N_5$.
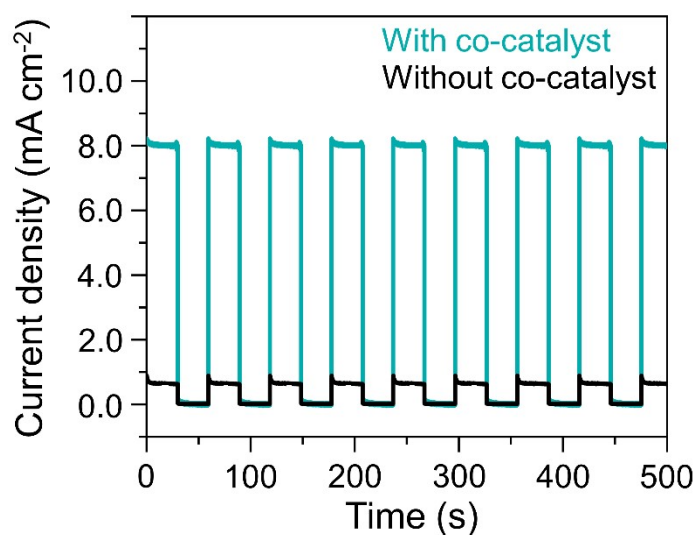

Figure S12. Chopped I-T Curve of $Cu,Zr_g-Ta_3N_5$ with or without $NiCoFe-B_i$ co-catalyst.
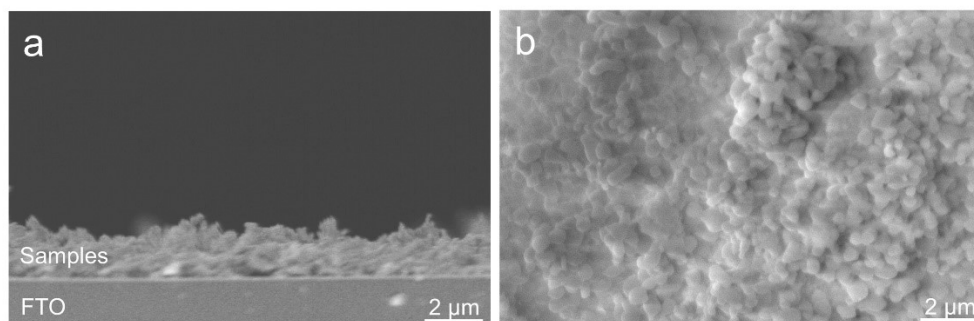
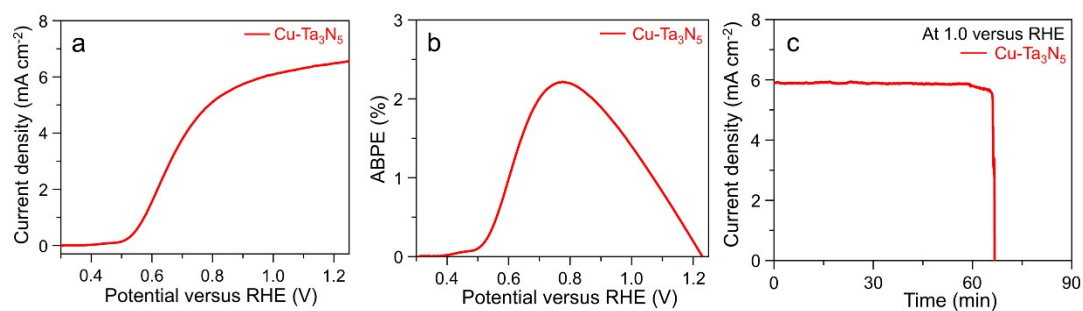Figure S13. a) Cross-sectional SEM image of $Cu,Zr_g-Ta_3N_5$; b) Top-view SEM image of $NiCoFe-B_i/Cu,Zr_g-Ta_3N_5$.

Figure S14. a) J-V curves for Cu-Ta$_3$N$_5$; b) ABPE of the Cu-Ta$_3$N$_5$ calculated from J-V curves from a; c) Steady-state photocurrent of Cu-Ta$_3$N$_5$ with NiCoFe-B$_i$ co-catalyst at 1.0 V versus RHE under AM 1.5G simulated sunlight.
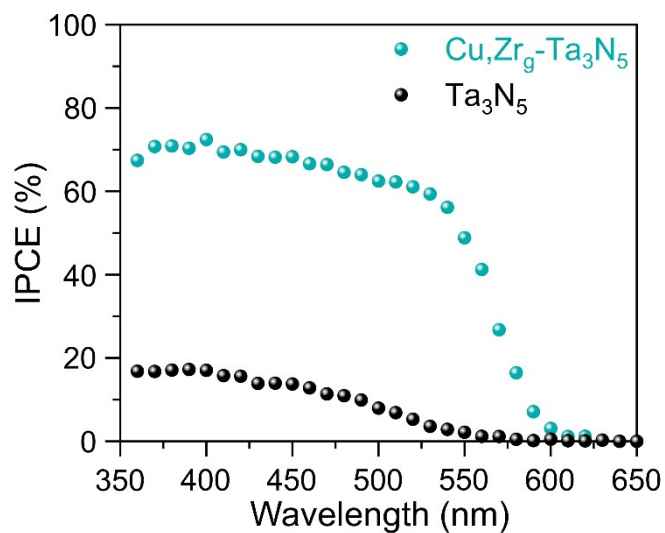

Figure S15. The IPCE spectrum of pristine Ta$_3$N$_5$ and Cu,Zr$_g$-Ta$_3$N$_5$.
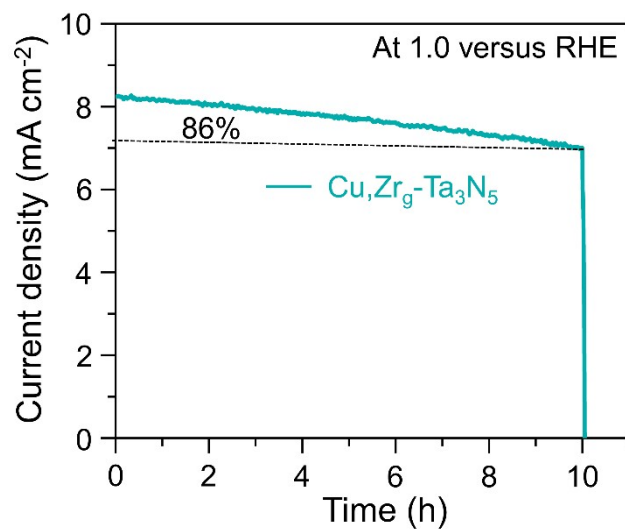
Figure S16. Stability of the photocurrent for NiCoFe-B$_i$/Cu,Zr$_g$-Ta$_3$N$_5$ photoanode at 1.0 V versus RHE under AM 1.5G in 1 M KOH.
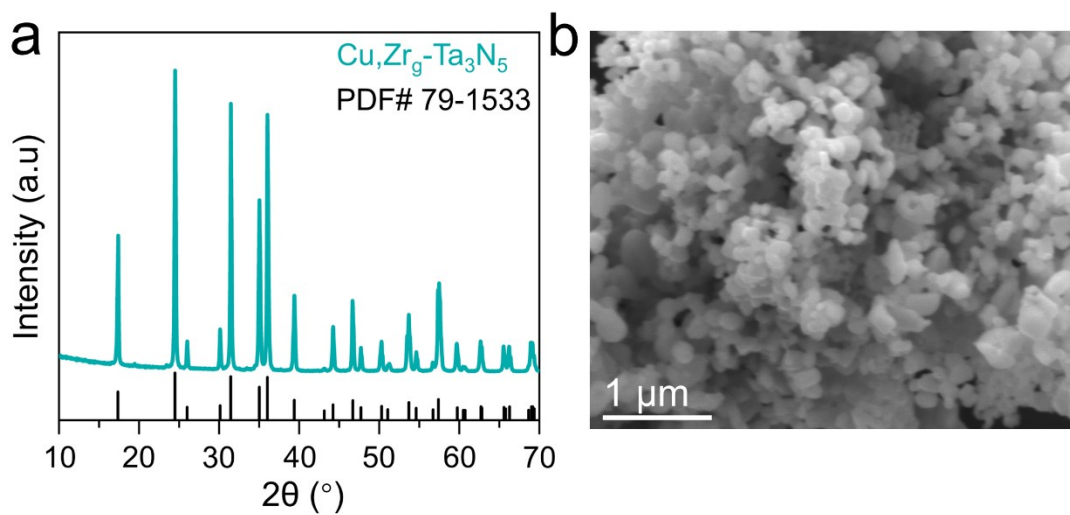
Figure S17. a) XRD pattern and b) SEM image for Cu,Zr$_g$-Ta$_3$N$_5$ after PEC water splitting test.

Figure S18. a) Ta 4*f*, b) N 1*s* and c) O 1*s* high-resolution XPS spectra of Cu,Zr$_g$-Ta$_3$N$_5$ after PEC water splitting test.
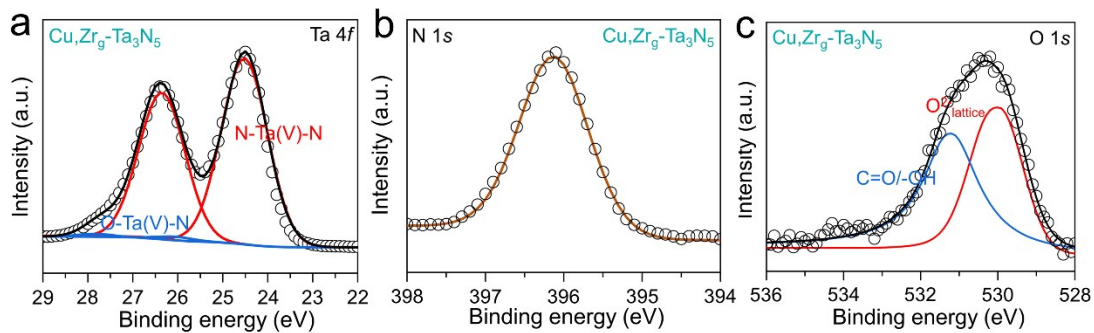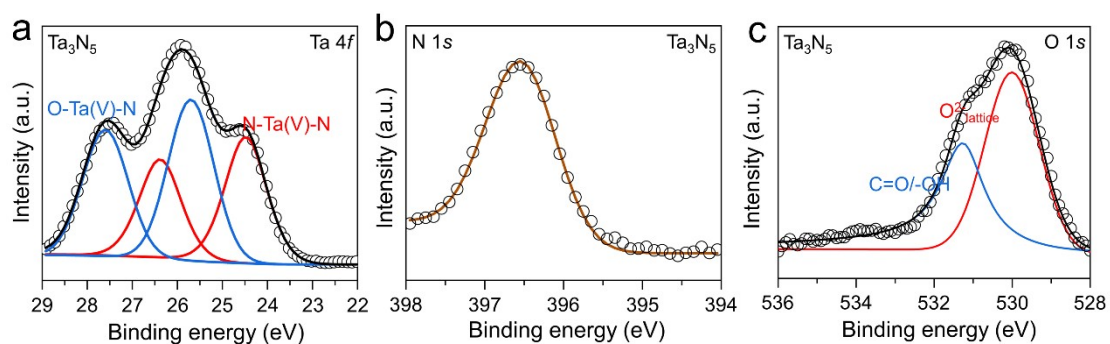

Figure S19. a) Ta 4*f*, b) N 1*s* and c) O 1s high-resolution XPS spectra of pristine Ta$_3$N$_5$ after PEC water splitting test.
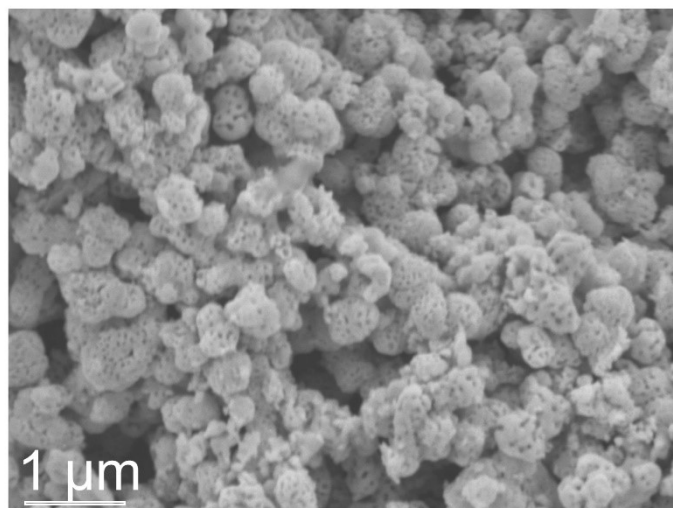

Figure S20. SEM image of pristine Ta$_3$N$_5$ after PEC water splitting test.

Table S1. Chemical compositions of Various Ta_3N_5 material as determined by ICP-AES and combustion analysis.

Sample	Weight ratio (wt%)/Atomic ratio (at%)				
	Ta^I	Cu^I	Zr^I	N^c	O^c
Cu,Zr_g-Ta_3N_5	80.1/30.9	5.4/5.9	1.2/0.9	9.8/48.8	3.1/13.5
Cu,Zr_h-Ta_3N_5	80.3/30.9	5.3/5.8	1.3/1.0	9.9/49.2	3.0/13.1
Cu-Ta_3N_5	82.5/32.8	5.1/5.8	0/0	11.1/57.0	1.0/4.5
Ta_3N_5	87.9/37.5	0/0	0/0	11.0/60.6	0.7/1.9

^{I} Measured by ICP-AES

^{c} Measured by the N-O combustion analyzer

Table S2. Bandgap and band positions of pristine Ta_3N_5, Cu-Ta_3N_5 and Cu,Zr_h-Ta_3N_5 photoanodes determined by UPS spectra and UV-vis absorption spectra.

Sample	E_{BG}(eV)	E_F(eV)	E_{VB}(eV)	E_{CB}(eV)
Pristine Ta_3N_5	2.06	-3.92	-5.97	-3.91
Cu-Ta_3N_5	2.08	-4.10	-5.99	-3.91
Cu,Zr_h-Ta_3N_5	2.10	-4.37	-6.31	-4.21

Table S3. Areas of the deconvoluted Ta $4f$ XPS peaks at specific binding energies.

Sample	Ta species								
	N-Ta(V)-N Peak area at B.E.=		Ratio	Ta^{3+} Peak area at B.E.=		Ratio	O-Ta(V)-N Peak area at B.E.=		Ratio
	24.5	26.4	(%)	23.6	25.5	(%)	26.0	27.9	(%)
Cu,Zr_g-Ta_3N_5	29353.0	22015.3	95.8	0	0	0	1277.4	958.1	4.2
Cu-Ta_3N_5	31996.7	23998.1	96.7	0	0	0	1083.3	812.5	3.3
Ta_3N_5	34655.7	25992.4	85.8	5068.7	3801.6	12.5	664.5	498.4	1.7

Table S4. Crystallite size of various Ta_3N_5 materials is obtained by applying Scherrer equation.

Peak position	Crystallite size (nm)				
	Pristine Ta_3N_5	Cu-Ta_3N_5	Zr-Ta_3N_5	Cu,Zr_h-Ta_3N_5	Cu,Zr_g-Ta_3N_5
(110)	33.3	31.8	32.4	36.2	41.8

Table S5. Fitted parameters for the TRPL decay of different Ta_3N_5 materials.

Sample	τ_1 (ns)	f_1	τ_2 (ns)	f_2	τ_{AV} (ns)	χ^2
Pristine-Ta_3N_5	0.11	93.25	2.34	6.75	0.26	1.049
Cu,Zr_h-Ta_3N_5	0.14	85.56	2.93	14.44	1.19	1.187
Cu,Zr_g-Ta_3N_5	0.21	65.11	3.65	34.89	1.41	1.119

The f_1 and f_2 are the fractional intensities; τ_1 and τ_2 are the lifetimes; τ_{AV} is the intensity-weighted average lifetime, which is equal to $f_1\tau_1 + f_2\tau_2$; and χ^2 is the reduced chi-square value.